PHYSICAL REVIEW B **82**, 104419 (2010)

Excess-electron induced polarization and magnetoelectric effect in yttrium iron garnet

Y. Kohara,[1] Y. Yamasaki,[1,*] Y. Onose,[1,2] and Y. Tokura[1,2,3]
[1]*Department of Applied Physics, University of Tokyo, Tokyo 113-8656, Japan*
[2]*Multiferroics Project, ERATO, Japan Science and Technology Agency (JST), Tokyo 113-8656, Japan*
[3]*Cross-Correlated Materials Research Group (CMRG) and Correlated Electron Research Group (CERG), ASI, RIKEN, Wako 351-0198, Japan*

(Received 20 July 2010; published 17 September 2010)

Magnetoelectric (ME) properties in yttrium iron garnet (YIG: $Y_3Fe_5O_{12}$), including both the first-order and second-order effects, have long been under dispute. In particular, the conflict between observations of the first-order ME effect and the centrosymmetric lattice structure has remained as a puzzling issue. As a key to solve the problem, we found that YIG shows quantum ME relaxation; the dielectric relaxation process is correlated closely with the magnetic one and has characteristic features of quantum tunneling. An application of magnetic field enhances the dielectric relaxation strength (by 300% at 10 K with 0.5 T), which gives rise to the large second-order ME (magnetocapacitance) effect critically dependent on the magnetization direction. The temperature and magnetic-field dependence of dielectric relaxation strength is well described by the noninteracting transverse-field Ising model for the excess-electron or Fe^{2+} center with the quantum tunneling and spin-orbit coupling effects. We could also spectroscopically identify such a ME Fe^{2+} center in terms of linear dichroism under a magnetic field along the specific direction. On this basis, the *fictitious* first-order ME effect—the magnetic-field induced electric polarization without the presence of external electric field—as observed for the electric-field cooled sample is ascribed to the combined effect of the above large second-order ME effect and the poling induced charge accumulation. The correlation between the ME effect and the thermally stimulated depolarization current indicates that hopping electrons freeze below around 125 K and the frozen-in dipoles generate an internal electric field (i.e., an electret-like effect). Investigation of electron-compensating doping effect on dielectric relaxation phenomena gives compelling evidences that excess electrons forming Fe^{2+} ions play a critical role in the charge accumulation as well as in the ME effect in YIG.

DOI: 10.1103/PhysRevB.82.104419 PACS number(s): 75.85.+t, 71.70.Ej, 75.50.Gg, 77.22.Ej

I. INTRODUCTION

Magnetoelectric (ME) effect is described as the change in magnetization by electric field [$(ME)_E$ effect] or of polarization by magnetic field [$(ME)_H$ effect]. This cross-correlated phenomenon has attracted considerable attention in recent years because of its novel physics and potential for practical applications.[1] Nevertheless, the correlation between magnetic and dielectric properties is usually very weak. One of the possible strategies to enhance the correlation is to target a family of multiferroics, in which ferroelectric and magnetic orders coexist. For example, the giant ME effect has been discovered in the materials that show the noncollinear spiral magnetic order.[2] In most of transverse-spiral magnets, magnetic order induces ferroelectricity[2–4] via the inverse Dzyaloshinskii-Moriya interaction or spin current mechanism[5,6] and such a ferroelectric state competes with another ME phase or domain. This phase/domain competition sometimes leads to a variety of ME effects; magnetic-field driven polarization flop/reversal,[3,4] terahertz electric-field driven magnetic resonance (electromagnon),[7] or change in dielectric constant by a magnetic field [magnetocapacitance (MC) effect].[8] Such multiferroicity is one of the promising routes to produce large ME coupling but is not the only one. In the preceding short paper,[9] we reported a large MC effect in the ferrimagnetic insulator, yttrium iron garnet (YIG) $Y_3Fe_5O_{12}$, and assigned it to magnetically tunable quantum paraelectricity. The underlying physics is unique but simple, and provide a new understanding of ME phenomena. In this paper, we report the full data supporting the coupling between the dielectric and the magnetic relaxations (MRs) and identify the microscopic origin of the large second-order ME effects. Furthermore, on this basis we argue the origin of the fictitious first-order ME effect that has long been in dispute.

The family of garnets has provided a fascinating field of science and technology because of versatile functions that could be attained by introducing different ions.[10] YIG is a typical material of garnets and widely used for technological application such as microwave devices or magneto-optical isolators. YIG has a cubic structure with the space group $Ia3d$ (Fig. 1): Fe^{3+} ions occupy two sites—the 16*a* octahedral sites and the 24*d* tetrahedral sites—and Y^{3+} ions are distributed over the 24*c* dodecahedral sites. YIG exhibits a ferrimagnetic order with the transition temperature of $T_N = 550$ K. Below T_N, the Fe spins of the *a* sites are antiparallel to those of *d* sites due to the superexchange interaction and along the magnetic easy axes $\langle 111 \rangle$ directions.

YIG has long been also known as a ME material.[11–13] O'Dell[11] observed that YIG shows the second-order $(ME)_H$ effect, which is equivalent to the MC effect and comes from the term $E_iE_jH_k$ in the free-energy expansion. The ME coefficient is enhanced during a magnetic domain rotation. Ogawa *et al.*[12] observed the first-order $(ME)_E$ effect in YIG below 125 K by applying an electric field during cooling. Further investigations by the same group, however, suggested this experimental result to be suspicious. Such emergence of the first-order ME effect conflicts the crystal symmetry of YIG (Ref. 13) and furthermore, significant sample

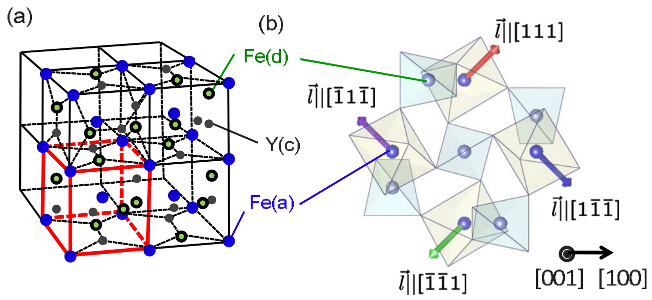

FIG. 1. (Color online) Crystal structure of $Y_3Fe_5O_{12}$. (a) Arrangement of cations in the garnet structure. (b) One eighth unit cell [red lines in (a)] showing the coordination of an oxygen ion. The arrows indicate trigonal symmetry axes in respective octahedral sites.

dependence was observed.[14] Up to now, there have been several publications which reported the broken inversion symmetry in YIG thin films or the related first-order ME effect.[15–17] Despite such many researches, the ME properties and mechanism in YIG has remained to be clarified.

The purpose of this paper is (i) to provide detailed experimental results to identify the origin of the second-order ME effect and (ii) to investigate the microscopic origin of the first-order ME effect. The paper is organized as follows. We first explain the essence of our model for the Fe^{2+} state as the ME-active center in Sec. II. Section III describes the sample preparation and the experimental setup. In Sec. IV, we present the experimental results and related discussions; the MC effect (Sec. IV A), the spectroscopic characterization of the ME Fe^{2+} center (Sec. IV B), and the electric-field cooling effect (Sec. IV C). Part of the experimental results on the MC effect (Sec. IV A) has been already published in a short paper.[9] Here, we present the full and systematic results of the MC effect, while avoiding the overlap of the data set shown in Ref. 9, to discuss its microscopic origin. Finally, concluding remarks are given in Sec. V.

II. MODEL OF Fe^{2+} SITE AS A MAGNETOELECTRIC CENTER IN YIG

As a microscopic origin of a novel ME response in YIG, we have proposed the impuritylike Fe^{2+}-state center endowed with the spin-orbit interaction.[9] To capture the feature, we employ the following transverse-field Ising model (TIM); a simple order-disorder type model based on a two-level system. The TIM was originally introduced by de Gennes to describe order-disorder type ferroelectrics.[18] The pseudospin formalism yields an Ising-type Hamiltonian of the form

$$\mathcal{H} = -\Omega \sum_i S_i^x - \Gamma \sum_i S_i^z, \tag{1}$$

where S^α denotes pseudospin-$\frac{1}{2}$ operator at ith dipole moment $\vec{\mu}$, Ω a transverse field which describes quantum-mechanical tunneling, and $\Gamma = \Delta + 2\mu E$ a longitudinal field with an energy difference due to a spontaneous energy splitting Δ and a coupling of the pseudospins to an external field E [Fig. 2(a)]. The thermal average of a pseudospin is

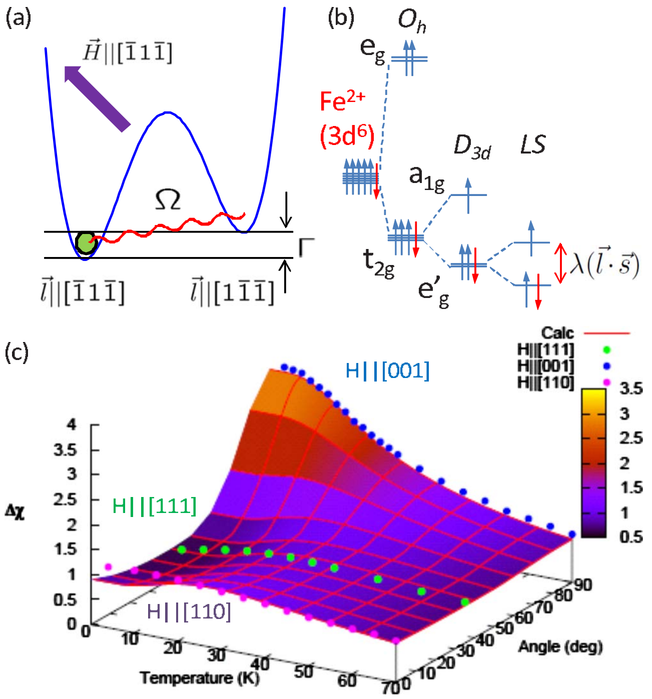

FIG. 2. (Color online) (a) Schematic illustration of quantum tunneling. Transverse field Ω and longitudinal field Γ are parameters describing quantum tunneling and an energy difference due to spontaneous energy splitting, respectively. (b) Energy diagram of $Fe^{2+}(3d^6)$ ion in an octahedral site. (c) Experimentally observed dependence of dc susceptibility (χ) on temperature and magnetization (M) direction (defined by the angle between the axis and M).The color plots are fitting results according to Eq. (4).

$$\langle \vec{S} \rangle = \frac{1}{2} \frac{\vec{F}}{|\vec{F}|} \tanh\left(\frac{|\vec{F}|}{2k_B T} \right) \tag{2}$$

with an effective field $\vec{F} = (\Omega, 0, \Gamma)$. The static polarization P and the susceptibility $\chi(=\varepsilon - 1)$ are calculated such as

$$P = \frac{n\mu\Gamma}{\sqrt{\Omega^2+\Gamma^2}} \tanh\left(\frac{\sqrt{\Omega^2+\Gamma^2}}{2k_B T} \right), \tag{3}$$

$$\chi = \frac{2n\mu^2\Gamma^2}{(\Omega^2+\Gamma^2)^{3/2}} \tanh\left(\frac{\sqrt{\Omega^2+\Gamma^2}}{2k_B T} \right) - \frac{n\mu^2\Gamma^2}{k_B T(\Gamma^2+\Omega^2)} \mathrm{sech}^2\left(\frac{\sqrt{\Omega^2+\Gamma^2}}{2k_B T} \right) \tag{4}$$

via $P = 2n\mu\langle S^z \rangle$ and $\varepsilon_0 \chi = (\partial P / \partial E)_{E=0}$. Here n denotes the number of dipoles (pseudospins) per volume and $\mu = |\vec{\mu}|$.

Despite its simplicity, the TIM has been successful in describing various systems. One example is quantum paraelectrics in which quantum fluctuations prevent pseudospin freezing or long-range ordering (even when pseudospin exchange interaction is introduced).[19] The degenerate case ($\Gamma = 0$) corresponds to the well-known Barret formula[20] with zero dipole-dipole interaction. χ increases with decreasing temperature, gradually deviates from the Curie law, and saturates at a low temperature. As increasing Γ, the energy splitting suppresses quantum dielectric fluctuations; χ shows a broad maximum and gently decreases with lowering temperature. In fact, electric-field induced polarized states and suppression of dielectric constant are realized in quantum paraelectric such as $SrTiO_3$ (Ref. 21) and $KTaO_3$.[22] The present idea to describe the ME coupling is that with exploiting the spin-orbit coupling the energy splitting Δ can be controlled in term of an external magnetic field H instead of electric field E.

Here we apply this idea to the case of the ME center of YIG. The excess electrons arising from oxygen vacancies play an important role in the emergence of MC effect in YIG. The excess electrons, when localized, induce a corresponding valence change from $Fe^{3+}(3d^5)$ to $Fe^{2+}(3d^6)$ ions. Considering their ion sizes, a small number of Fe^{2+} ions are expected to reside on the octahedral a sites.[10] Energy diagram of $Fe^{2+}(3d^6)$ ion on an octahedron site [Fig. 2(b)] is a key to control the energy level splitting via the spin-orbit coupling. In a cubic crystal field (~1 eV) of O_h symmetry, the Fe 3d states are split into lower t_{2g} and higher e_g levels. On the octahedron positions, the oxygen ions are trigonally distorted around these sites with D_{3h} symmetry and their symmetry axis coincides with one of the ⟨111⟩ [Fig. 1(b)]. This trigonal crystal field (~0.1 eV) leads to a further separation of cubic t_{2g} levels into a singlet a_{1g} and a doublet e'_g. For Fe^{2+} characterized by an unquenched angular momentum, the doublet is further split due to a spin-orbit coupling $[\lambda(\vec{l}\cdot\vec{s})]$ between the angular momentum $(\vec{l})$ pointing to the respective symmetry axes and the spin $(\vec{s})$. There are four nonequivalent octahedral sites distinguished by the orientation of symmetry axes along different ⟨111⟩ directions. Therefore, the energy-level difference Γ among these nonequivalent octahedral sites depends on the direction of magnetization and hence the dielectric fluctuation can be controlled by an external magnetic field H.

This model can actually describe the magnetic and thermal behaviors of quantum dielectric relaxation (DR) in YIG.[9] The dots in Fig. 2(c) shows the experimentally observed dependence of the dielectric relaxation strength $\Delta\chi$ on temperature and magnetic field ($H\parallel[001]$, [111], and [110]; see Sec IV A). The color plot in Fig. 2(c) are fitting results according to Eq. (4) with the parameters $n\mu^2/\varepsilon_0=135$ K and $\Omega=42$ K. Here, Γ is calculated as the average value of the energy-level difference due to the spin-orbit coupling among the octahedron sites (e.g., $\Omega=42$ K and $\Gamma=0$ K for $H\parallel[001]$).

In Sec. IV A, we show the experimental date to confirm the validity of this model; (i) the dielectric fluctuation of YIG can be expressed by the TIM and (ii) Fe^{2+} ions play an important role in the emergence of MC effect in YIG. In Sec. IV B, we present the spectroscopic characterization of such a ME Fe^{2+} center.

III. EXPERIMENT

Single crystals of YIG were grown by the traveling solvent floating zone (TSFZ) technique.[23] The starting polycrystalline material was prepared by a standard solid-state reaction method from high-purity powders of Y_2O_3 (99.9%) and Fe_2O_3 (99.9%). The stoichiometric mixture was ground and calcined at 1300 °C for 10 h in air. The resulting powder was pressed hydrostatically into a cylindrical rod of 5–10 mm in diameter and 70 mm long and sintered in oxygen gas at 1350 °C for 15 h. The crystal growth by the TSFZ method was performed in flowing oxygen atmosphere with the growth speed of 1.0 mm/h and the rotation speed of 20 rpm. In order to avoid incongruent melting to form orthoferrite ($YFeO_3$), the composition with $Fe_2O_3:Y_2O_3=85:15$ was employed as a solvent. The single crystals were oriented using Laue x-ray diffraction patterns, and cut into thin plates with the widest faces perpendicular to the [100] direction. Typical sample size was 10 mm^2 in area and 1 mm in thickness. Silver electrodes were evaporated onto the widest faces of the sample for electric measurements. Dielectric constants were measured by an *LCR* meter (Agilent E4980A) and an impedance/gain phase analyzer (Solartron 1260) equipped with a dielectric interface (Solartron 1296). The current was measured by an electrometer (Keithley 8517A). The change in an electric polarization ΔP was obtained by integrating the pyroelectric or ME current as a function of time. The dc magnetization and magnetic ac susceptibility (10 Hz–10 kHz) were measured using a superconducting quantum interference device magnetometer (Quantum Design). For optical (transmittance and reflectivity) measurements, the sample was thinned to about 100 μm and polished to mirrorlike surfaces with alumina powder. Optical spectrum was measured with the grating-type monochrometer for the photon energy range of 0.5–1.8 eV. Sample was mounted in a helium flow-type optical cryostat and a Halbach magnet was used to apply the magnetic field (~0.35 T).

IV. RESULTS AND DISCUSSION

A. Second-order magnetoelectric (magnetocapacitance) effect

Here we present the observation and characterization of the second-order ME effect in terms of MC measurement. Figure 3 shows the magnetic field (H) dependence of (a) magnetization (M), (b) dielectric constant (ε) at various measuring frequencies, and (c) change in an electric polarization $[\Delta P(E_{bias})]$ with various bias electric fields (E_{bias}) at 10 K. H was applied parallel to the [100] direction in all cases. For measurements of ε and ME current, the electric field (E) and the probed polarization current were also parallel to the [100] direction. The M-H curve displays the ordinary magnetization behavior and saturates around 0.3 T. The saturated magnetic moment at 10 K is 5.1 μ_B/f.u., consistent with the expected saturation moment of YIG. As seen in Fig. 3(b), ε shows a sudden increase in the vicinity of H where M is saturated. Furthermore, the H induced change in ε depends strongly on the measurement frequency. The relative change in ε $\{[\varepsilon(1T)-\varepsilon(0T)]/\varepsilon(0T)\}$ at 10 Hz exceeds 10% but the MC effect is no more discernible at 100 kHz. The MC effect is essentially equivalent to the second-order ME effect and can be also detected through the direct measurement of ME current with applying an electric field [Fig. 1(c)]. $\Delta P(E_{bias})$ is proportional to E_{bias}, as expected. The proportionality coefficient $\Delta P(E_{bias})/E_{bias}$ corresponds to the

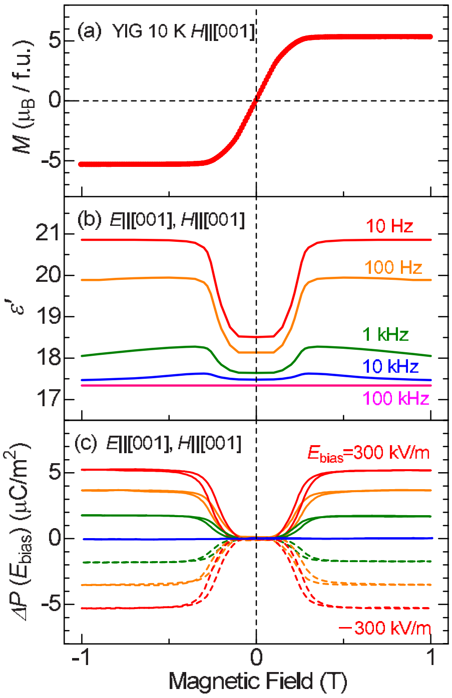

FIG. 3. (Color online) Magnetic-field dependence of (a) magnetization (M), (b) dielectric constant (ε, 10–100 kHz), and (c) change in an electric polarization [$\Delta P(E_{bias}), -300 \leq E_{bias} \leq 300$ kV/m] at 10 K. H and E were applied parallel to [100] directions.

change in ε in the low-frequency limit, i.e., the static permittivity. In fact, $\Delta P(E_{bias})(1T)/\varepsilon_0 E_{bias} \sim 2.0$ (ε_0 being vacuum permittivity) is nearly the same value as change in ε at 10 Hz [$\varepsilon(1T)-\varepsilon(0T)=2.4$]. $\Delta P(E_{bias})$ shows a small hysteresis with increasing and decreasing H, which reflects the response retardation of M against the H sweep (0.01 T/s).

The frequency-dependent MC effect [Fig. 3(b)] suggests that the relaxation dynamics may correlate closely with ME effects. Therefore, we have investigated magnetic-field dependence of the DR. Figure 4 shows the evolution of the dielectric spectra with increasing H at 10 K [(a) real and (b) imaginary parts of dielectric constant $\varepsilon = \varepsilon' + i\varepsilon''$] and (c) corresponding Cole-Cole (ε' vs ε'') plots. The dielectric spectra are not of dispersion type but of relaxation type while the Cole-Cole plots show the derivation from an ideal semicircle. It is known that many dielectric relaxation processes occasionally deviate in reality from the simple Debye model and can be described by the following empirical equation (Havriliak-Negami equation):[24]

$$\varepsilon^*(\omega) = \varepsilon_\infty + \frac{\Delta\varepsilon}{[1+(i\omega\tau)^\beta]^\alpha}. \tag{5}$$

Here, ε_∞ is the permittivity at the high-frequency limit, $\Delta\varepsilon = \varepsilon_s - \varepsilon_\infty$ is the relaxation strength where ε_s is the static permittivity, and τ is the characteristic relaxation time. α and β are parameters which characterize the asymmetry and broadness of the corresponding spectra. The experimental data are well fitted with Eq. (5) [Fig. 4(c)]. Magnetic-field dependence of fitting parameters α, β, and $\Delta\varepsilon$ is shown in Fig. 4(d). We can see that the frequency-dependent MC effect originates from the H induced variation in $\Delta\varepsilon$ ($H<0.5$ T) and α ($H>0.5$ T). $\Delta\varepsilon$ shows large enhancement by an application of magnetic field (300% at 0.5 T). α takes low values ($\sim$0.68) at 0 T, increases with increasing H even after the magnetization saturates, and reaches 0.95 at 3 T. On the other hand, β remains constant ($\sim$0.87) independent of magnetic field.

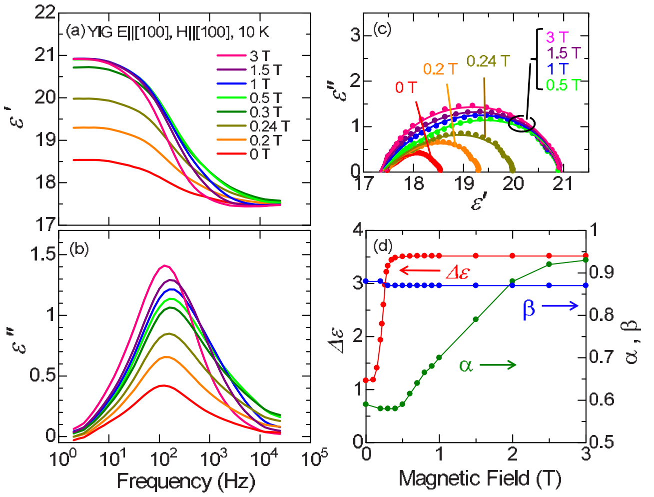

FIG. 4. (Color online) [(a) and (b)] Dielectric spectra at 10 K under various magnetic fields. (a): real part (ε') and (b) imaginary part (ε''). (c) Cole-Cole plots (ε' vs ε'') at selected magnetic fields. The solid lines are fitting results according to Havriliak-Negami equation [Eq. (5)]. (d) Magnetic-field dependence of fitting parameters: Havriliak-Negami parameters (α, β) and relaxation strength ($\Delta\varepsilon$).

The ME effect in YIG shows anisotropic properties with respect to the H direction (Fig. 5). Figure 5(a) shows the dependence of $\Delta P(E_{bias})$ on H applied along three different directions ([001], [110], and [111]). The ME effect is not observed when H is applied along the [111] direction while that for $H \| [110]$ is smaller in magnitude than that for $H \| [001]$; the difference in the saturation field of ΔP reflects that of M. Anisotropic properties of the ME effect are clearly seen by the measurement of ΔP in response to rotation of H. We chose the configuration so that H is rotated within the $(\bar{1}10)$ plane; ϕ is defined by the angle between the H vector and the [001] direction. Figure 5(b) shows ΔP as a function of ϕ, measured at $H=0.05-0.3$ T with $E_{bias}=500$ kV/m.

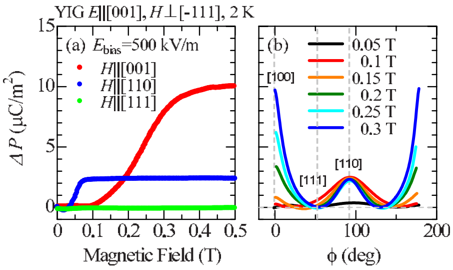

FIG. 5. (Color online) (a) $\Delta P(E_{bias})$ vs H along three different directions ([001], [110], and [111]) at 2 K. (b) ΔP measured in H rotating within the $(\bar{1}10)$ plane. ϕ denotes the angle between H vector and [001] direction.

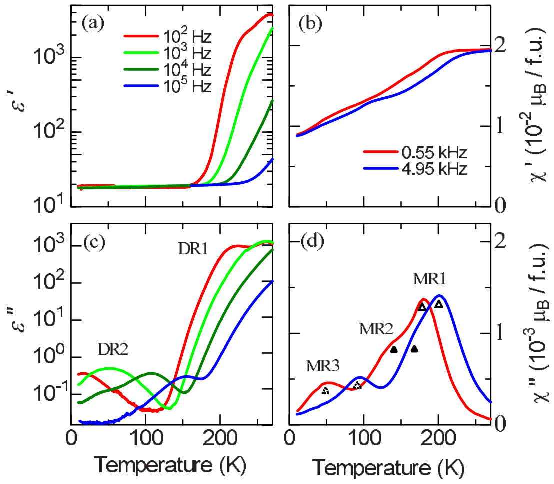

FIG. 6. (Color online) Temperature dependence of (a) real part (ε') and (b) imaginary part (ε'') of dielectric permittivity (ε), (c) real part (χ') and (d) imaginary part (χ'') of magnetic susceptibility at various frequencies.

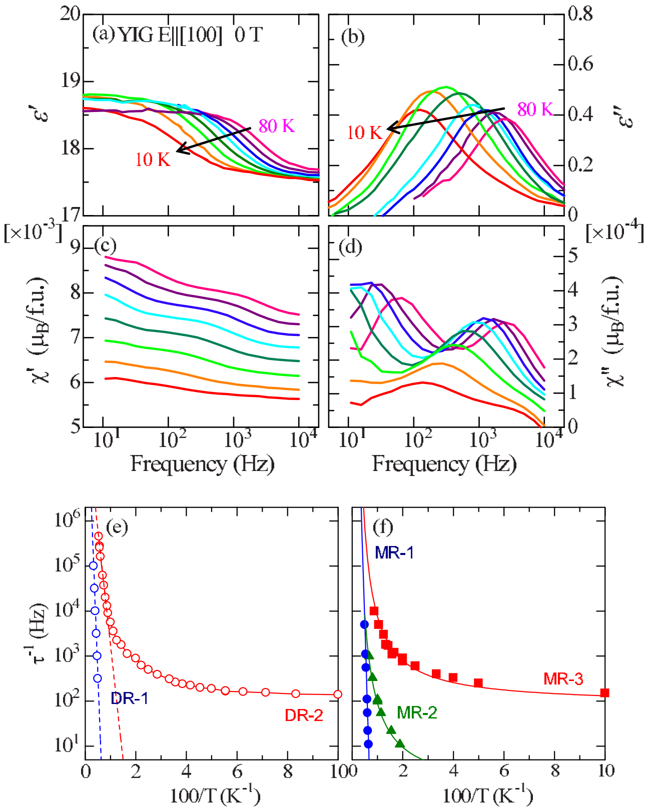

FIG. 7. (Color online) [(a) and (b)] Dielectric and [(c) and (d)] ac magnetic susceptibility spectra with 10 $K \leq T \leq 80$ K. Arrhenius plot for (e) DRs and (f) MRs. The straight lines present Arrhenius behavior with the parameters given in the text.

ΔP shows a periodic change with the cycle of 180°. The direction of Fe spin moment ($\vec{M}$) is supposed to be parallel to H at the field larger than 0.3 T because the saturated moment of M is isotropic along all crystallographic axes. Considering this result and also the fact that the magnetic easy axis lies along the $\langle 111 \rangle$ direction, ΔP can be described as

$$\Delta P = E_{bias}[\varepsilon(\vec{M}) - \varepsilon(\vec{M} \parallel [111])]. \tag{6}$$

Figures 6(a) and 6(b) show the temperature dependence of ε' and ε'' at various frequencies. ε' and ε'' show the typical signature of relaxational behavior. ε' exhibits a steplike increase from a certain temperature. The step shifts to higher temperature with increasing frequency while accompanied by a peak in ε''. As seen in Fig. 6(b), two DRs were observed below room temperature. The higher temperature DR (DR1) shows up above 150 K and its large relaxation strength is on the order of 1000 while the lower temperature DR (DR2) shows up below 125 K and its relaxation strength is three orders of magnitude smaller than that of DR1. We have also observed some relevant MR phenomena. Figures 6(c) and 6(d) show the temperature dependence of real (χ') and imaginary (χ'') parts of magnetic ac susceptibility. We found three distinct MRs (MR1, MR2, and MR3) below room temperature (at enough lower temperatures than the ferrimagnetic transition).

For understanding of the physical nature of the relaxation dynamics, the evolution of DR and MR with varying temperature are plotted in Figs. 7(a)–7(d). Additionally, we plot the relaxation rates of DR and MR against the inverse temperature in Figs. 7(e) and 7(f). The high-temperature relaxations DR1 and MR1 exhibit a thermally activated behavior as described by the Arrhenius law,

$$\tau(T) = \tau_0 \exp(E_a/k_B T), \tag{7}$$

where τ_0 is the Debye relaxation time in the high-temperature limit, E_a an activation energy, and k_B the Boltzmann constant. From the slope of the fitted straight lines in Figs. 7(e) and 7(f), E_a=0.29 eV is obtained in common to DR1 and MR1. DR1 and MR1 are commonly ascribed to polaron hopping process accompanying charge transfer between Fe^{2+} and Fe^{3+} ($Fe^{2+} \leftrightarrow Fe^{3+} + e^-$).[25,26] All the irons in stoichiometric YIG are ferrous (Fe^{3+}) ions and a possible cause of the presence of ferric (Fe^{2+}) ions is oxygen vacancies in the lattice; the thermal activation (E_a=0.29 eV) is not for the electron (polaron) density but for its hopping process.

As decreasing temperature, the dielectric and magnetic responses, DR1 and MR1, finally freeze up, while Arrhenius plot of DR2 and MR3 provide a clear evidence for significant deviations from the thermally activated behavior at lower temperatures; the relaxation rate is almost independent of temperature below 10 K and remains finite ($\tau^{-1} \sim 100$ Hz) even at the lowest temperature (2 K). Such a behavior is characteristic of quantum-mechanical tunneling and has been similarly observed in quantum paraelectrics [e.g., $SrTiO_3$,[27] $K_{1-x}Li_xTaO_3$,[28] and $Ba_{1-x}Nd_xCeO_3$ (Ref. 29)]. Moreover, the temperature-dependent relaxation rate of DR2 coincides with that of MR3, indicating the magnetoelectric nature that the respective relaxations are strongly coupled with each other. Concerning MR in YIG, Torres *et al.*[30] and Walz *et al.*[31] had intensively investigated in terms of the magnetic aftereffect phenomena. They also found three relaxations in YIG below room temperature and argued that these processes would be associated with the existence of magnetically anisotropic Fe^{2+} ions, in contrast to isotropic

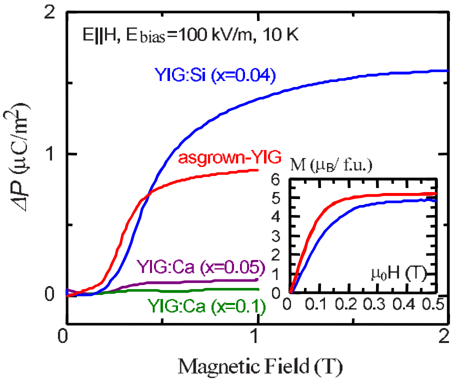

FIG. 8. (Color online) Second-order magnetoelectric effect in as-grown YIG, YIG:Si ($x=0.04$) and YIG:Ca ($x=0.05,0.1$). Here, x represents a nominal composition of dopant in the forms of $Y_3Fe_{5-x}Si_xO_{12}$ and $Y_{3-x}Ca_xFe_5O_{12}$. The inset shows M-H curves for as-grown YIG and YIG:Si.

Fe^{3+} ions. As discussed in Sec. II, the spin-orbit coupling energy of Fe^{2+} ion in each nonequivalent octahedral site depends on the direction of magnetization. Therefore, the magnetization change gives rise to the rearrangement of these ions through an electron exchange between Fe^{2+} and Fe^{3+} ions so as to minimize the free enthalpy of the system, which is expected to contribute to the magnetic relaxation. Moreover, the local exchange of respective Fe-ion valences is equivalent to the reorientation of an electric dipole, which gives rise to the dielectric relaxation. It is known that this kind of polarized center sometimes shows quantum tunneling phenomena.[32,33] Summing up these results, the existence of Fe^{2+} ions in YIG plays a crucial role in emergence of both magnetic and dielectric relaxations, which arise from the quantum tunneling of excess electron at low temperatures.

YIG can be doped with tetravalent or divalent impurities, and an introduction of these impurities is expected to change the valence of Fe ions. Therefore, we have attempted to compensate/introduce excess electrons by impurity doping. Figure 8 represents ME effect on as-grown YIG, YIG doped with Ca, and YIG doped with Si. The ME effect as observed in as-grown YIG is totally negated in Ca-doped YIG (nominal formula of $Y_{3-x}Ca_xFe_5O_{12}$; $x=0.05$), which viewed as electron-compensated YIG. On the other hand, the enhancement of ME effect is observed in Si-doped YIG ($Y_3Fe_{5-x}Si_xO_{12}$; $x=0.04$), which is viewed as electron-doped YIG. These results imply that the emergence of MC effect as well as relaxation phenomena requires excess electrons. In the case of as-grown (nonintentionally doped) YIG, excess electrons are donated perhaps by oxygen vacancies.[34]

As for the origin of the MC effect, the ME coupling through elastic strain (magnetostriction mechanism) is ruled out for the present case because the magnetostriction constant in YIG is rather small [$\lambda \sim 8\times10^{-6}$ (Ref. 35)]. Furthermore, the present observation of the concurrent magnetic relaxation and the anisotropic properties of ME effect also exclude the possibility that the frequency-dependent MC effect would arise through a combination of magnetoresistance and the Maxwell-Wagner effect, unrelated to the true ME coupling.[36] We thus conclude that noninteracting transverse-field Ising model including tunneling and spin-orbit coupling terms (Sec. II) explains the MC effect in YIG; the quantum ME relaxation hosted by impuritylike Fe^{2+} ions can be controlled by magnetic field through the spin-orbit interaction.

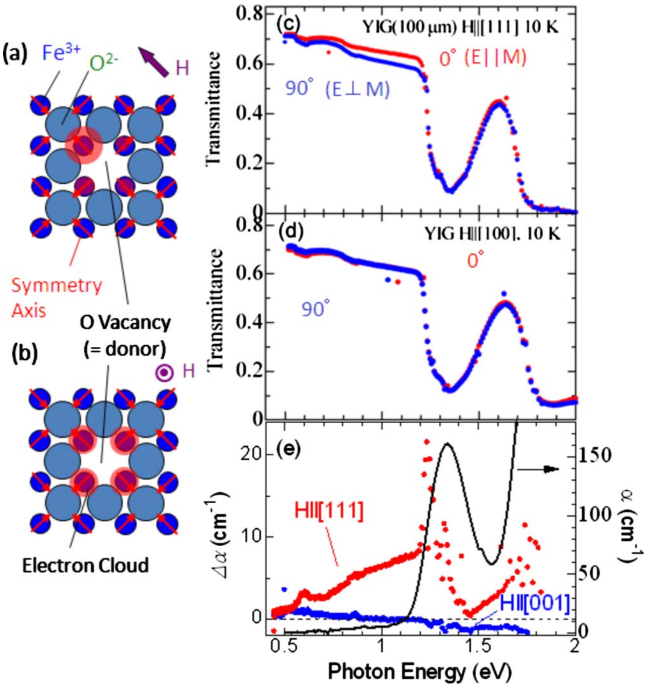

FIG. 9. (Color online) Schematic picture of electron cloud around the oxygen vacancy for (a) $H\|[111]$ and (b) $H\|[001]$. The arrows drawn on the Fe^{3+} sites indicate the trigonal symmetry axes. Transmittance spectra of YIG with $E\|M$ and $E\perp M$ at 10 K for (c) $H\|[111]$ and (d) $H\|[100]$. (e) Absorption coefficient α and LD spectra ($\Delta\alpha$) for $H\|[111]$ and $H\|[001]$.

B. Spectroscopy of magnetoelectric Fe^{2+} site

As discussed in Secs. II and IV A, the MC effect in YIG originates from H induced change in the site occupancy of excess electrons through the quantum tunneling and spin-orbit coupling. In this section, we spectroscopically characterize ME Fe^{2+} center in terms of linear dichroism (LD) measurement under a magnetic field. LD is defined as the difference in absorption of light polarized parallel and perpendicular to an orientation axis ($\Delta\alpha$) and has been used to investigate site symmetries of color center (localized electrons in insulators).[37] H induced change in LD properties is anticipated for the present ME Fe^{2+} center because of the following reasoning: the application of $H\|[111]$ urges the excess electron to form the Fe^{2+} state on an octahedral site with $l\|[111]$ (the lowest energy site among four nonequivalent octahedral sites) and should cause the LD in Fe^{2+}-related electronic absorption. [see Fig. 9(a)]. On the other hand, in the case of the quadruply degenerate state for $H\|[001]$, the centers are equally distributed in all possible directions and hence will show isotropic absorption [see Fig. 9(b)]. Figures 9(c) and 9(d) show transmittance spectra of YIG with $E\|M$ and $E\perp M$ at 10 K for $H\|[111]$ and $H\|[001]$, respectively. The magnetic iron garnets are transparent in the range 0.2–1.0 eV (a window region). Above 1.0 eV the absorption in-

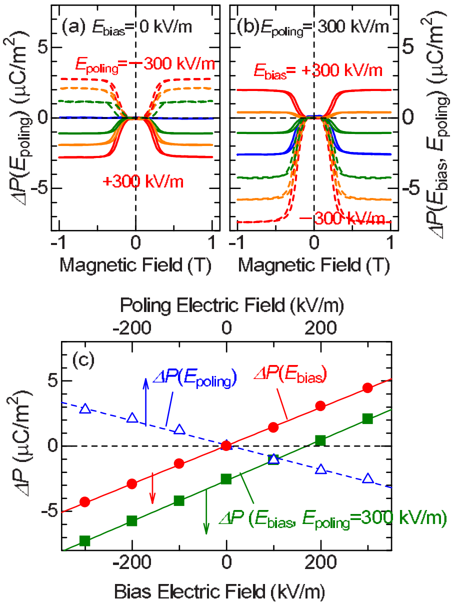

FIG. 10. (Color online) Magnetic-field dependence of (a) $\Delta P(E_{poling})$ (b) $\Delta P(E_{bias},E_{poling})$ at 10 K. (c) Electric-field dependence of $\Delta P(E_{bias})$, $\Delta P(E_{poling})$, and $\Delta P(E_{bias},E_{poling})$.

creases progressively because of the electronic transitions between the Fe^{3+}($3d^5$) levels the peak at 1.2 eV corresponds to the $^6A_{1g}\rightarrow{}^4T_{1g}$ transition Fe^{3+} ion on the octahedral sublattice.[38] As shown Figs. 9(c) and 9(d), the magnitude of LD depends markedly on the direction of the applied magnetic field as expected; LD can be observed for $H\parallel[111]$ while no more discernible for $H\parallel[001]$. This confirms that the Fe center has the symmetry axis that can lie along any one of the four $\langle 111\rangle$ directions. The LD spectra ($\Delta\alpha$ vs photon energy) for $H\parallel[111]$ and $H\parallel[001]$ is shown in Fig. 9(e). The broad peak is observed around 1.0 eV at the LD spectra for $H\parallel[111]$, making a clear distinction from the Fe^{3+} $^6A_{1g}\rightarrow{}^4T_{1g}$ absorption centered at 1.3 eV. It is noticeable that the difference of the absorption spectra between pure-YIG and Si-doped YIG (Ref. 39) shows the similar structure to the LD spectra. This suggests that LD is related with Fe^{2+} ions, not with Fe^{3+} ions. Summarizing these results, the LD in YIG consistent is with our interpretation of the ME effect and thus we could spectroscopically identify such a ME Fe^{2+} center.

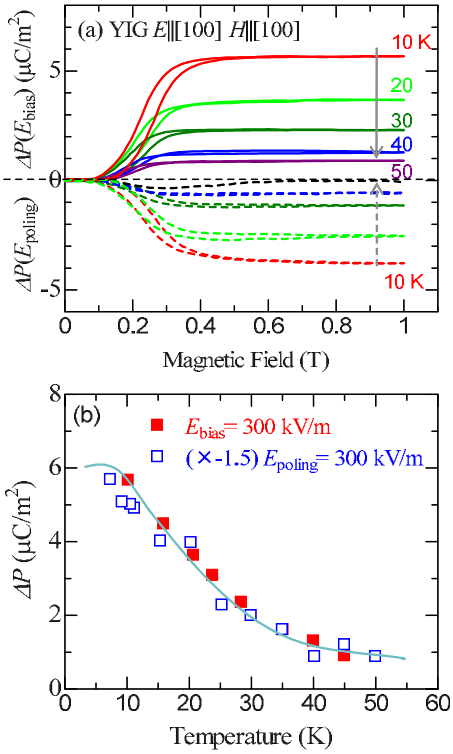

FIG. 11. (Color online) (a) Magnetic-field dependence of $\Delta P(E_{bias})$ and $\Delta P(E_{poling})$ at selected temperatures. (b) Temperature dependence of $\Delta P(E_{bias})(1T)$ and $\Delta P(E_{poling})(1T)$.

C. Fictitious first-order magnetoelectric effect

In this section, we discuss the origin of first-order ME effect. In Ref. 12, it was reported that first-order ME effect was observed below 125 K when a sample was cooled in an electric field. This motivated us to investigate the effect of electric-field cooling on ΔP (Fig. 10). We use different notations, $\Delta P(E_{bias})$, $\Delta P(E_{poling})$, and $\Delta P(E_{bias},E_{poling})$, to distinguish settings of measurement, as follows. In the case of $\Delta P(E_{bias})$, a sample is cooled down without an electric field but a bias electric field is applied in the measurement. $\Delta P(E_{poling})$ is measured with a poling procedure and without applying a bias electric field, and $\Delta P(E_{bias},E_{poling})$ is measured with a poling procedure and applying a bias electric field. Poling temperature (T_{poling}), from which the field cooling (E_{poling}) is started, is 180 K in all cases. Figure 10(a) shows H dependence of $\Delta P(E_{poling})$ with various poling electric fields (E_{poling}). Conventionally, the H induced generation of ΔP without electric field (E_{bias}) as observed is reminiscent of the first-order ME effect of the polar (ferroelectric) magnet but we have noticed the following evidences against the first-order ME effect. The proportionality between E_{poling} and $\Delta P(E_{poling})$ holds well and the absolute value of $\Delta P(E_{poling})/\varepsilon_0 E_{poling}\sim 1.3$ is comparable to (only slightly smaller than) $\Delta P(E_{bias})/\varepsilon_0 E_{bias}\sim 2.0$. Furthermore, the behaviors of $\Delta P(E_{bias})$ and $\Delta P(E_{poling})$ are similar to each other apart from the opposite sign. In Fig. 10(b), H dependence of $\Delta P(E_{bias},E_{poling})$ with $E_{poling}=300$ kV/m and varying E_{bias} is shown. We found that E_{bias} and E_{poling} affect ME effect independently and that $\Delta P(E_{bias},E_{poling})$ is described as

$$\Delta P(E_{bias},E_{poling})=\Delta\varepsilon(E'_{bias}). \tag{8}$$

Here, the *effective* bias field is defined as $E'_{bias}=E_{bias}-E'_{poling}$; $-E'_{poling}$ is the *effective* internal field generated by the poling procedure. We summarize the values of $\Delta P(1T)$ in Fig. 10(c) as determined from Figs. 3(c), 10(a), and 10(b). Fitting these results with Eq. (8) suggests that $E'_{poling}\sim 0.65E_{poling}$; therefore, $\Delta P(E_{poling})$ represents not the first-order ME effect but the second-order one as well as $\Delta P(E_{bias})$. Figure 11 shows the temperature dependence of $\Delta P(E_{bias})$ and $\Delta P(E_{poling})$. ΔP becomes measurable around 60 K and increases with decreasing temperature. Equation (8) holds at all temperatures below 60 K.

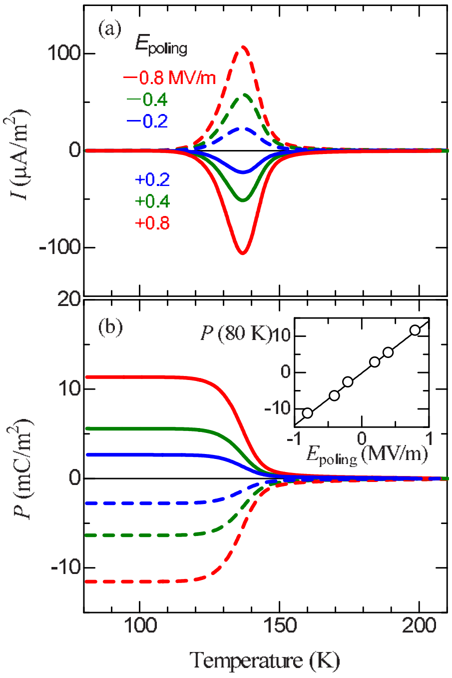

FIG. 12. (Color online) Temperature dependence of (a) pyroelectric current I and (b) polarization P (derived from I) with various poling fields (E_{poling}). Inset to (b): E_{poling} vs P(80 K).

To clarify the effect of the electric-field cooling, we performed measurements of pyroelectric current. In Fig. 12, the pyroelectric current (I) and polarization (P) as a function of temperature with various poling electric fields (E_{poling}) are shown. In all cases, T_{poling} is 180 K and the heating rate is 0.1 K/s. In the temperature-increasing run, I begins to flow around 110 K, reaches maximum at 130 K, and then decreases back to zero. P is proportional to E_{poling} [Fig. 12(b) inset] and reaches 10 mC/m^2 at $E_{poling}=0.8$ MV/m. This value is larger by six orders of magnitude than $\Delta P(E_{poling})$ and comparable to a spontaneous polarization of ferroelectric materials (e.g., 260 mC/m^2 in BaTiO$_3$). The emergence of the pyroelectric current cannot be ascribed to a ferroelectric phase transition because no anomaly is observed in ε [Fig. 6(a)]. Such a transition was not detected by past studies with x ray, electron diffraction, or Mössbauer spectroscopy.[13] The observed phenomena can be understood in terms of thermally stimulated depolarization current (TSDC).[40,41] A plausible scenario is as follows.

When the poling electric field is applied at relatively high temperatures, barely mobile charge carriers (Fe^{2+}-like polaron) tend to distribute so as to screen the electric field. As the temperature is lowered, the charge carriers become trapped with such a distribution. Since the relaxation time is infinitely long at enough low temperatures, an internal electric field by the frozen-in dipoles persists even after the removal of an external electric field. The phenomenon is analogous to an electret effect.[42] This internal field is the origin of E'_{poling} or $\Delta P(E_{poling})$. Thermally activated release of trapped carriers during the heating procedure contributes to TSDC. Incidentally, the inequality that $E'_{poling} \sim 0.65 E_{poling}$ as observed implies some loss (35%) or recombination of trapped charges in cooling the sample from T_{poling}(=180 K) to the lowest temperature (10 K).

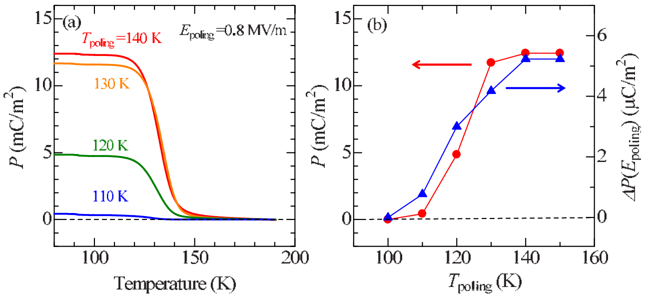

FIG. 13. (Color online) (a) Temperature dependence of P with various T_{poling} (b) T_{poling} dependence of $P(E_{poling})$(80 K) and $\Delta P(E_{poling})(1T)$ with $E_{poling}=300$ kV/m.

The correlation between TSDC and ME effects is clearly seen in Fig. 13, which plots the T_{poling} dependence of the built-in polarization (P) and the ME component [$\Delta P(E_{poling})$]. Both P and $\Delta P(E_{poling})$ decrease sharply around $T_{poling}=120$ K, which indicates that the redistribution charges can be spatially fixed below 120 K.

The TSDC measurement is a major probe for the study on the dielectric relaxation dynamics and used to obtain the relaxation parameters. In the Bucci-Fieschi-Guidi framework,[40] which assumes that a system has a single relaxation time $\tau(T)$ and the decay rate of P (polarization current I) is proportional to P, P is described by the following differential equation:

$$\frac{dP}{dt} = -\frac{P}{\tau(T)}. \tag{9}$$

Adopting Arrhenius law [Eq. (7)], we deduce

$$\ln \tau(T) = \frac{E}{k_B T} + \ln \tau_0 = \ln\left[-\frac{1}{I(T)}\int_T^{\infty} I(T)dT\right]. \tag{10}$$

Using Eq. (10), we can obtain $\tau(T)$ from TSDC. In Fig. 14(a), we plot $\log \tau(T) = \log[P(T)/I(T)]$ vs the inverse temperature. The broken line shows the Arrhenius behavior with the best-fit parameter $E=0.28$ eV.

The polarization current (I) can be written as a function of T to solve Eq. (9),

$$I(T) = -\frac{dP}{dt} = \frac{P_0}{\tau(T)}\exp\left[-\frac{1}{b}\int_{T_0}^{T}\frac{1}{\tau(T)}dT\right], \tag{11}$$

where P_0 is the equilibrium polarization, $b=dT/dt$ the heating rate, and T_0 the initial temperature. By differentiation with T, the relation between b and T_m at which I peaks is derived as

$$\ln\frac{T_m^2}{b} = \frac{E}{k_B T_m} + \ln\frac{\tau_0 E}{k_B}. \tag{12}$$

In Fig. 13(b), the heating rate (b) dependence of TSDC is shown. As expected from Eq. (12), T_m shifts to lower temperature with decreasing the heating rate. We determined the values of parameters for Eq. (12) by the least-square fitting to obtain the activation energy, $E=0.38$ eV [see the inset of Fig. 14(b)]. The activation energy of TSDC agrees with that of DR1 and MR1, again confirming that the polaron (Fe^{2+}

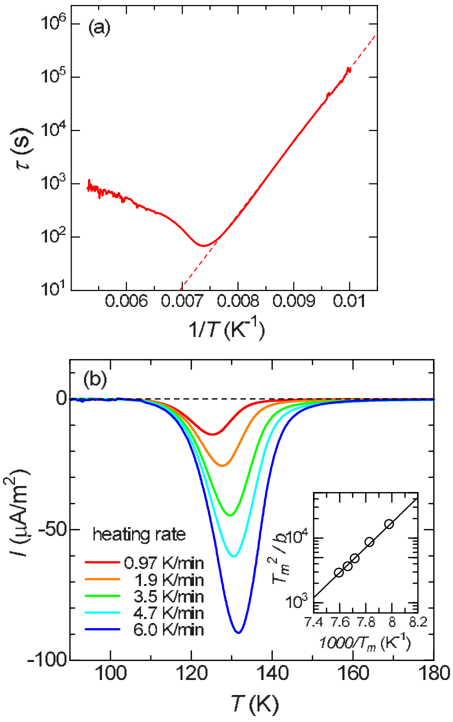

FIG. 14. (Color online) (a) log $\tau = \log(P/I)$ vs the inverse temperature (T^{-1}) [Eq. (10)] (b) heating rate ($b = dT/dt$) dependence of TSDC.

species) hopping, trapping, and freezing process are relevant to the observed P and TSDC.

V. CONCLUSIONS

We have carried out a comprehensive investigation of ME properties in YIG. First, we discussed the mechanism of MC effect in YIG in Sec. IV A. In the floating zone method for the crystal growth, the crystals are exposed to somewhat reducing atmosphere during growth, and therefore may contain an appreciable quantity of Fe^{2+} ions. Fe^{2+} ions have been known to cause various effects such as photomagnetic effect[10,43] and magnetic annealing effect,[44] and also play an important role in the emergence of MC effect inYIG. The excess electrons hopping among the octahedral a sites would give rise to the dielectric relaxation. An application of magnetic field enhances the dielectric relaxation strength, which gives rise to the large MC effect. The important findings of the present study are (i) dielectric relaxation has a characteristic feature of quantum-mechanical relaxation at low temperatures and (ii) dielectric relaxation has the same relaxation time as the magnetic relaxation caused by magnetically anisotropic $Fe^{2+}(3d^6)$ ions. The quantum-mechanical relaxation can be controlled by the magnetic field through the spin-orbit interaction mediated tuning of state degeneracy; accordingly, the permittivity changes according to the direction of the magnetization. We also confirmed the magnetic-field induced change in the linear dichroism which is consistent with this scenario as shown in Sec. IV B. This mechanism may be applied to the various systems. One good candidate is a material with spinel structure in which there are also four equivalent octahedral sites distinguished by four different $\langle 111 \rangle$ directions of distortion. Our finding clearly demonstrates that our microscopic model not only can reveal the possible coupling mechanism in YIG but also paves the way to exploring the ME effect in the magnetic quantum paraelectric system.

As a closely relevant issue, we discussed the origin of puzzling first-order ME effect in YIG in Sec. IV C. By performing the electric-field poling procedure, we can observe the fictitious first-order ME effect without a bias electric field, as accompanied by huge pyroelectric current. The emergence of pyroelectric current does *not* originate from a ferroelectric phase transition but can be understood in terms of TSDC. The correlation between ME effect and TSDC indicates that hopping electrons freeze thermally around 125 K and the frozen-in dipoles generate an internal electric field. This internal electric field has a negative sign with respect to the poling electric field and causes the first-order ME effect in YIG. The analysis of TSDC data shows that activation energy of TSDC agrees with the ones of dielectric and magnetic relaxations which are ascribed to polaron hopping process accompanying charge transfer between Fe^{2+} and Fe^{3+}. This finding gives a negative conclusion of the phase transition around 125 K and can solve the long-standing mystery of the fictitious first-order ME effect in YIG.

ACKNOWLEDGMENTS

We would like to thank N. Oda, H. Murakawa, F. Kagawa, and N. Kida for their help in measurements and H. Katsura, N. Nagaosa, and T. Arima for fruitful discussions. This work was supported in part by Grants-In-Aid for Scientific Research (Grants No. 15104006, No. 17340104, and No. 16076205) and also by the Funding Program for World-Leading Innovative R&D on Science and Technology (FIRST Program) from the MEXT of Japan and JSPS.

---

*Present address: Photon Factory, Institute of Materials Structure Science, KEK, Tsukuba 305-0801, Japan.

[1] M. Fiebig, J. Phys. D **38**, R123 (2005).
[2] S. W. Cheong and M. Mostovoy, Nature Mater. **6**, 13 (2007); Y. Tokura and S. Seki, Adv. Mater. **22**, 1554 (2010).
[3] T. Kimura, T. Goto, H. Shintani, K. Ishizaka, T. Arima, and Y. Tokura, Nature (London) **426**, 55 (2003).
[4] Y. Yamasaki, S. Miyasaka, Y. Kaneko, J. P. He, T. Arima, and Y. Tokura, Phys. Rev. Lett. **96**, 207204 (2006).
[5] I. A. Sergienko and E. Dagotto, Phys. Rev. B **73**, 094434 (2006).
[6] H. Katsura, N. Nagaosa, and A. V. Balatsky, Phys. Rev. Lett. **95**, 057205 (2005).
[7] A. Pimenov, A. A. Mukhin, V. Yu. Ivanov, V. D. Travkin, A. M. Balbashov, and A. Loidl, Nat. Phys. **2**, 97 (2006).

[8] F. Kagawa, M. Mochizuki, Y. Onose, H. Murakawa, Y. Kaneko, N. Furukawa, and Y. Tokura, Phys. Rev. Lett. **102**, 057604 (2009).

[9] Y. Yamasaki, Y. Kohara, and Y. Tokura, Phys. Rev. B **80**, 140412(R) (2009).

[10] *Physics of Magnetic Garnets*, edited by A. Paoletti (North-Holland, Amsterdam, 1978).

[11] T. H. O'Dell, Philos. Mag. **16**, 487 (1967).

[12] H. Ogawa, E. Kita, Y. Mochida, K. Kohn, S. Kimura, A. Tasaki, and K. Shiratori, J. Phys. Soc. Jpn. **56**, 452 (1987).

[13] S. Hirakata, M. Tanaka, K. Kohn, E. Kita, K. Siratori, S. Kimura, and A. Tasaki, J. Phys. Soc. Jpn. **60**, 294 (1991).

[14] E. Kita, S. Takano, K. Kohn, K. Siratori, S. Kimura, and A. Tasaki, J. Magn. Magn. Mater. **104-107**, 449 (1992).

[15] B. B. Krichevtsov, V. V. Pavlov, and R. V. Pisarev, JETP Lett. **49**, 535 (1989).

[16] R. V. Pisarev, B. B. Krichevtsov, V. N. Gridnev, V. P. Klin, D. Frohlich, and Ch. Pahlke-Lerch, J. Phys.: Condens. Matter **5**, 8621 (1993).

[17] V. V. Pavlov, R. V. Pisarev, A. Kirilyuk, and Th. Rasing, Phys. Rev. Lett. **78**, 2004 (1997).

[18] P. G. de Gennes, Solid State Commun. **1**, 132 (1963).

[19] K. A. Müller and H. Burkard, Phys. Rev. B **19**, 3593 (1979).

[20] J. H. Barrett, Phys. Rev. **86**, 118 (1952).

[21] J. Hemberger, P. Lunkenheimer, R. Viana, R. Bohmer, and A. Loidl, Phys. Rev. B **52**, 13159 (1995).

[22] G. A. Sawara, Jpn. J. Appl. Phys., Suppl. **24**, 80 (1985).

[23] S. Kimura and I. Shindo, J. Cryst. Growth **41**, 192 (1977).

[24] S. Havriliak and S. Negami, Polymer **8**, 161 (1967).

[25] Y. J. Wu, Y. Gao, and X. M. Chen, Appl. Phys. Lett. **91**, 092912 (2007).

[26] H. Sekizawa, S. Iida, and T. Miyadai, J. Phys. Soc. Jpn. **13**, 658 (1958).

[27] R. Viana, P. Lunkenheimer, J. Hemberger, R. Bohmer, and A. Loidl, Phys. Rev. B **50**, 601 (1994).

[28] W. Kleemann, V. Schonknecht, D. Sommer, and D. Rytz, Phys. Rev. Lett. **66**, 762 (1991).

[29] I. Kuskovsky, B. S. Lim, and A. S. Nowick, Phys. Rev. B **60**, R3713 (1999).

[30] C. Torres, O. Alejos, J. M. Munoz, P. Hernandez-Gomez, and C. de Francisco, Phys. Rev. B **66**, 024410 (2002).

[31] F. Walz, J. H. V. J. Brabers, L. Torres, and H. Kronmuller, Phys. Status Solidi B **228**, 717 (2001).

[32] V. Narayanamurti and R. O. Pohl, Rev. Mod. Phys. **42**, 201 (1970).

[33] I. G. Austin and N. F. Mott, Adv. Phys. **50**, 757 (2001).

[34] Annealing procedure in oxygen gas/vacuum is expected to compensate/introduce oxygen vacancies. We have tried several annealing procedures (varying annealing temperatures, times, and gas species) for our single-crystal sample, however, the annealing procedure was turned out not to be effective as the chemical doping/compensative procedure.

[35] A. E. Clark, H. B. Callen, E. R. Callen, B. Desavage, and W. Coleman, J. Appl. Phys. **34**, 1296 (1963).

[36] G. Catalan, Appl. Phys. Lett. **88**, 102902 (2006).

[37] D. L. Staebler and S. E. Schnattery, Phys. Rev. B **3**, 516 (1971).

[38] D. L. Wood and J. P. Remeika, J. Appl. Phys. **37**, 1232 (1966).

[39] J. F. Dillon, Jr., E. M. Gyorgy, and J. P. Remeika, J. Appl. Phys. **41**, 1211 (1970).

[40] C. Bucci, R. Fieschi, and G. Guidi, Phys. Rev. **148**, 816 (1966).

[41] Gorur G. Raju, *Dielectrics in Electric Field* (Marcel Dekker, New York, 2003).

[42] G. M. Sessler, *Electrets* (Springer-Verlag, Berlin, 1987).

[43] J. F. B. Hawkes and R. W. Teale, J. Phys. C **5**, 481 (1972).

[44] R. P. Hunt, J. Appl. Phys. **38**, 2826 (1967).